AIAA JOURNAL
Vol. 30, No. 2, February 1992

Planar Laser-Induced Fluorescence Imaging of Shock-Tube Flows with Vibrational Nonequilibrium

B. K. McMillin,* M. P. Lee,* and R. K. Hanson†
Stanford University, Stanford, California 94305

Single-shot planar laser-induced fluorescence images of nitric oxide in shock-heated flows with vibrational nonequilibrium are reported. The results demonstrate that planar laser-induced fluorescence imaging is a promising diagnostic technique for multidimensional high-speed flows because of its ability to examine shock structure and to visualize and measure vibrational nonequilibrium. The flows studied were generated within a shock tube and were composed of dilute mixtures of NO in argon. A narrow-band ArF laser tuned to the $D \leftarrow X$ (0,1) R_2 (28.5) transition of NO at 193.346 nm was used as the excitation source. The broadband fluorescence was collected at 90 deg to the path of excitation using an intensified, two-dimensional photodiode array. Images presented include a normal incident shock, a normal reflected shock, and a four-image sequence of the development of high-temperature supersonic flow over a two-dimensional blunt body. The vibrational relaxation in the downstream region of the normal shocks is analyzed and compared with calculations based on known relaxation rates.

Introduction

PLANAR laser-based imaging techniques are becoming an increasingly important diagnostic tool for investigating both reacting and nonreacting gas flows. These methods are particularly attractive because they can provide spatially and temporally resolved property measurements and flowfield visualization of a planar region. Although planar measurements are not sufficient to fully characterize complex three-dimensional flows, they can provide quantitative information and resolve flow structures that may be obscured with conventional line-of-sight optical techniques. Planar laser-induced fluorescence (PLIF) is both species- and quantum-state-specific and thus is capable of measuring multiple flowfield properties including species concentration, temperature, pressure, and velocity.[1,2] The combination of these features along with its excellent spatial and temporal resolution makes PLIF a very powerful diagnostic technique for investigating complex supersonic/hypersonic flows.

Here, we report the first application of PLIF imaging to nitric oxide, NO, in nonreacting shock-tube flows with vibrational nonequilibrium. (Preliminary results were reported previously for both molecular oxygen[3] and nitric oxide.[4,5]) The effects of vibrational nonequilibrium are prominent in many aerodynamic applications including hypersonic flight and atmospheric re-entry studies. Thus, the ability to probe nonequilibrium effects with a combustion/high-temperature air species such as NO is of considerable importance.

Shock-tube flows provide a well-characterized environment for the development and verification of PLIF as a nonequilibrium flow diagnostic. The vibrational relaxation in these one-dimensional flows is well understood, relatively simple to model, and readily measured with conventional techniques, such as laser absorption[6] or infrared emission.[7] Although the primary results of the present study were obtained in these simple flows, they clearly demonstrate the potential of PLIF imaging to simultaneously probe nonequilibrium and visualize shock-wave structure in more complex multidimensional flows.

In the following sections, the theory of PLIF and the spectroscopy of NO for excitation near 193 nm are briefly reviewed. In addition, the experimental facility is described, the spatial resolution of the imaging system is discussed, and representative imaging results are presented. Single-shot PLIF images of both normal incident and reflected shocks in dilute mixtures of NO in argon are examined. The vibrational relaxation of NO in the downstream region of these shocks is analyzed and compared to calculations based on known relaxation rates. In addition, a four-image sequence illustrating the temporal development of high-temperature supersonic flow over a two-dimensional blunt body is presented and discussed.

Technique

Theory

In a typical PLIF experiment, a thin sheet of pulsed laser light is used as an excitation source, with the wavelength tuned to coincide with a particular rovibronic transition of a species in the flow of interest. The laser sheet is directed through the flow and the resulting fluorescence from the illuminated region is imaged onto a two-dimensional solid-state camera, recorded, and later processed using a computer. The fluorescence signal is integrated temporally, but the laser pulse duration and fluorescence lifetimes are sufficiently short to provide flow-stopping temporal resolution. Various flowfield properties can be determined from the images through their known dependence on the fluorescence signal, or from the relative signals obtained by excitation and detection of multiple transitions.

In general, the fluorescence signal depends on the pressure, temperature, species concentration, and laser intensity and will reflect vibrational nonequilibrium through a dependence on the absorbing state population. Assuming a broad laser source with respect to the absorption linewidth and applying a simple steady-state rate equation analysis, we can write[8]

$$R_f \propto \chi N F(T,T_v) I_\nu / [I_\nu + I_\nu^{\text{sat}}] \qquad (1)$$

where R_f is the local fluorescence rate (photons/s), χ the mole fraction of the absorbing species, N the total number density,

Presented as Paper 90-1519 at the AIAA 21st Fluid Dynamics, Plasma Dynamics, and Lasers Conference, Seattle, WA, June 18–20, 1990; received June 27, 1990; revision received Feb. 4, 1991; accepted for publication Feb. 6, 1991.

*Graduate Research Assistant, High Temperature Gasdynamics Laboratory, Department of Mechanical Engineering. Student Member AIAA.

†Professor, High Temperature Gasdynamics Laboratory, Department of Mechanical Engineering. Member AIAA.

F the Boltzmann fraction of the absorbing state, T the translational/rotational temperature, T_v the vibrational temperature, I_ν the spectral laser intensity, and I_ν^{sat} the saturation intensity, which depends on the Einstein coefficients and various quenching rates.

The simple nonreacting flows considered here generally consist of two distinct regions separated by a shock wave. Within a given region, the local number density and translational/rotational temperature do not vary significantly, whereas the vibrational temperature varies considerably due to the shock-induced vibrational nonequilibrium. Thus, the fluorescence signal variation within a given region is primarily determined by the evolving absorbing state vibrational population, i.e., $R_f \propto F(T_v)$. However, the magnitude of the fluorescence signal in a given region (i.e., on either side of the shock) depends not only on the thermodynamic state of the gas, but also on the collisional quenching (and predissociation) rates in that region.

By selectively exciting a transition from a single vibrational level, the axial fluorescence distribution in the one-dimensional flow behind a normal shock wave provides a measure of the vibrational relaxation of the absorbing species. (Note that, although the shock heating actually results in the population of excited vibrational levels, this process is conventionally described as vibrational relaxation, i.e., relaxation toward the new equilibrium distribution.) The vibrational relaxation rate obtained in this manner is that of the absorbing state vibrational level. However, this individual vibrational relaxation rate can be related to the relaxation rate of the overall vibrational energy by assuming that the gas continuously maintains a Boltzmann distribution.

In the previous discussion, we have assumed that either the test gas is optically thin or the laser intensity is sufficient to saturate the transition (i.e., $I_\nu >> I_\nu^{sat}$). If the laser intensity is not sufficient to saturate the transition, the fluorescence signal is dependent on the laser energy, and any spatial laser energy variation will correspondingly affect the fluorescence signal. This is not a problem in the optically thin limit because no significant intensity variations are introduced by absorption. However, if the test gas is not optically thin, the fluorescence signal at a given location can be significantly influenced by the laser attenuation prior to that point. Hence, because the measured fluorescence profile along any given streamline depends on the vibrational relaxation and the spatial distribution of the laser intensity, variations in the laser intensity distribution due to attenuation can distort the relaxation rate inferred from the fluorescence signal.

In contrast, for saturated excitation where $I_\nu >> I_\nu^{sat}$, the fluorescence signal is independent of laser intensity. Thus, assuming the transition remains saturated across the imaged region, laser intensity variations due to absorption will not affect the signal and the fluorescence profile will accurately reflect the vibrational relaxation.

Nitric Oxide Spectroscopy

Excimer lasers operating on ArF at 193 nm have been used to access a variety of NO transitions. Shibuya and Stuhl[9] first demonstrated broadband ArF laser excitation of NO at 193 nm. Wodtke et al.[10] later demonstrated the use of tunable narrowband ArF lasers for excitation of the $B^2\Pi \leftarrow X^2\Pi$ (7,0) and $D^2\Sigma^+ \leftarrow X^2\Pi$ (0,1) transitions of NO. In the $B \leftarrow X$ (7,0) band, rotational levels ranging from $J'' = 23.5$ to 34.5 can be directly excited with an ArF laser, whereas in the $D \leftarrow X$ (0,1) band, accessible levels range from $J'' = 17.5$ to 45.5. Rovibronic transitions of $A^2\Sigma^+ \leftarrow X^2\Pi$ (3,0) and (4,1) bands can also be excited near 193 nm, but these transitions are typically weaker than those of the $D \leftarrow X$ and $B \leftarrow X$ bands.

In order to investigate the usefulness of ArF excitation for PLIF imaging of NO, excitation spectra of heated NO have been obtained. Nitric oxide (0.5%) diluted in N_2 was flowed through an electric torch (Sylvania model SGH 014-372), and the resultant peak temperature of the gas exiting the torch was ~1000 K. The narrowband output from an ArF laser (Lambda Physik model EMG 150 MSC) was apertured down to a 0.5-mm spot and propagated through the heated NO/N_2 flow. A lens was used to focus the resultant NO fluorescence at right angles to the path of excitation onto a uv-sensitive solar-blind photomultiplier tube (Hamamatsu R166UH). A 2-mm-thick UG-5 Schott glass filter was used to block the scattered laser light while passing the broadband NO fluorescence at longer wavelengths. The wavelength of the laser was scanned by rotating the laser grating using a motor-driven micrometer, and the photomultiplier tube output was averaged using a boxcar averager (Stanford Research Systems model SR-280). The laser was operated at 30 Hz and the wavelength was tuned at a rate of ~0.001 nm/s. The spectra were obtained by averaging 30 laser shots while the laser was scanning.

A typical NO excitation spectrum is shown in Fig. 1a, and a calculated NO absorption spectrum at 1000 K is shown for comparison in Fig. 1b. Line identifications are shown for the prominent lines in the $D \leftarrow X$ (0,1) band and for the isolated lines in the $B \leftarrow X$ (7,0) band. Note that, because Fig. 1a is an excitation spectrum and Fig. 1b is an absorption spectrum, we do not expect the relative strengths of the spectral lines in the two plots to match. However, we do expect correspondence between the calculated and observed line positions, and for this, we do see good agreement. In addition, note that the spectral lines are broader and that overlaps occur in the excitation spectrum as a result of the relatively broad laser spectral profile.

The baseline signal in the measured excitation spectrum results from the weak excitation of NO by the residual broadband component of the narrowband laser spectral output.[11] The baseline is lowest near the center of the ArF gain curve at 193.34 nm where the locking efficiency is highest. Near the limits of the ArF tuning range, the locking efficiency decreases and, consequently, the baseline signal increases.

In the imaging results presented later, we chose to excite a $D \leftarrow X$ (0,1) transition for a number of reasons. For example, because the ground vibrational state of this band is vibrationally excited ($v'' = 1$), the resulting fluorescence signal is very sensitive to changes in vibrational temperature. Such sensitivity makes this band ideal for studies of vibrational nonequilibrium in supersonic flows. Also, the oscillator strength and Einstein A coefficient for this band are at least an order of magnitude greater than for any other NO transition accessible using 193-nm excitation; consequently, $D \leftarrow X$ excitation provides the strongest fluorescence signal.

Although not used here, we should also note that the overlapping transitions of the $D \leftarrow X$ (0,1) band at 193.369 nm, i.e., P_1 (39.5), Q_1 (32.5), and R_1 (26.5), are isolated from the nearby lines of the Schumann-Runge bands of O_2 in this wavelength region.[10] Hence, these transitions can be used to probe NO in the presence of O_2 without the complication of separating the O_2 and NO fluorescence signals. This may be an important consideration in future aerodynamic or combustion studies where both NO and O_2 are present and 193-nm excitation is used.

Once NO is excited to the D state, several de-excitation paths are possible and depend, in general, on what other species are present. An NO energy-level diagram illustrating the important de-excitation paths following $D \leftarrow X$ excitation in the presence of argon is shown in Fig. 2. In the figure, W_{XD} and W_{DX} are the stimulated absorption and emission rates, A_{ij} is the Einstein coefficient for spontaneous emission from state i to state j, Q_{ij}^{Ar} is the Ar-NO collisional quenching rate from state i to state j, Q_i^{NO} is the NO-NO collisional quenching rate from state i to all lower states, and Q_P is the predissociation rate of NO from the C state. Note that the B state is not included in the diagram because its participation in D state de-excitation is not significant in NO/Ar mixtures.[12] Be-

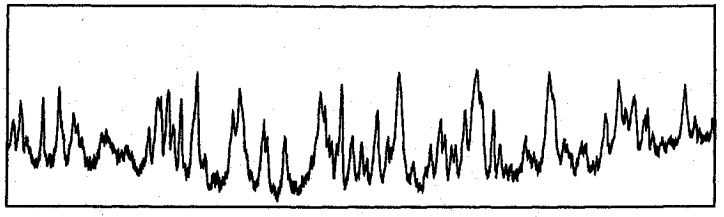

Fig. 1a Excitation spectrum of NO measured with broadband collection.

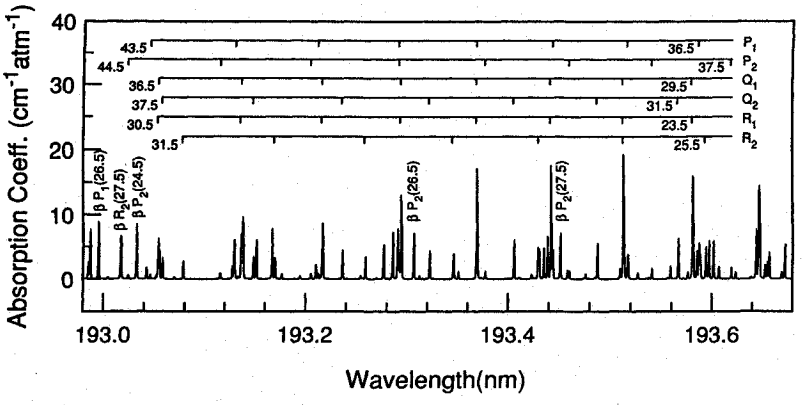

Fig. 1b Calculated absorption spectrum for NO near 193 nm assuming T = 1000 K, P = 1 atm, and a collisional linewidth of 0.055 cm^{-1}. The prominent $D \leftarrow X$ lines and the prominent, isolated $B \leftarrow X$ or β-lines are labeled in the absorption spectrum.

sides the $D \rightarrow X$ fluorescence and quenching paths, NO can fluoresce from the D to the A state and, subsequently, the A state can either fluoresce or collisionally quench to the X state.

Nitric oxide molecules in the D state can also collisionally quench to the C state and lead to $C \rightarrow X$ fluorescence, as observed by Wodtke et al.[10] in the measured fluorescence spectrum of a flame following $D \leftarrow X$ excitation. In the presence of argon, collisional quenching to the C state is one of the key de-excitation paths for NO in the D state. Argon quenches the D state to the C state exclusively, and does so very efficiently, with a rate that is 60% of the gas-kinetic collision rate for NO and argon.[13] Following this de-excitation, the C state NO molecules can predissociate or can fluoresce or self-quench to either the A or the X state. Note that in this study the collisional quenching from the C state is predominantly NO-NO self-quenching because argon does not significantly quench NO from the C state.[13]

Although a fluorescence spectrum was not measured in this study, the spectral emission distribution can be estimated (at least qualitatively) from the relative magnitudes of the rates for the important excitation and de-excitation processes. Table 1 summarizes the relevant emission, predissociation, and quenching rates for the conditions of this study (T = 1000–3000 K, P = 0.5–3 atm, 0.5–1% NO in argon). The quenching rates listed were estimated assuming the quenching cross sections reported by Callear and Pilling[12] do not vary with temperature. Using these rates and applying a simple rate equation analysis, we find that the majority of the emission is composed of comparable amounts of $D \rightarrow X$ and $C \rightarrow X$ fluorescence (187–268 nm), whereas the fluorescence contribution from $A \rightarrow X$ is considerably weaker.

The significant amount of $C \rightarrow X$ fluorescence expected here results from the indirect population of the C state through the efficient quenching of NO from the D to the C state by argon, combined with the relatively weak predissociation of the v = 0 level of the C state. Note, however, that, although the $C \rightarrow X$ fluorescence is shifted ~920 cm^{-1} to the red, it has the same general spectral character as that of $D \rightarrow X$ fluorescence because of their similar Frank-Condon factors.

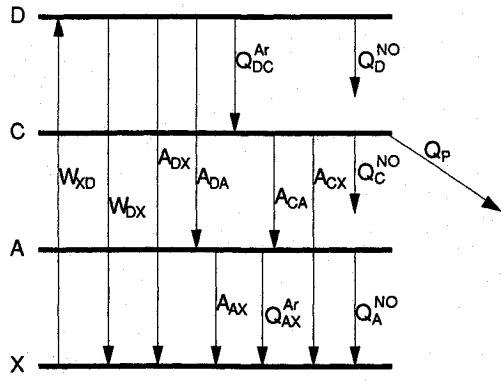

Fig. 2 Energy-level diagram for NO including the X, A, C, and D electronic states: the arrows show the important de-excitation processes following $D \leftarrow X$ excitation in the presence of argon.

Table 1 Important excitation and de-excitation rates

Process	Rate coefficient, s^{-1}
W_{XD}	~10^{10}
W_{DX}	$2W_{XD}$
A_{DX} (v' = 0)	4.1 × 10^7
A_{DA} (v' = 0)	0.95 × 10^7
A_{CX} (v' = 0)	5.1 × 10^7
A_{CA} (v' = 0)	3.5 × 10^7
A_{AX} (v' = 0)	0.51 × 10^7
Q_{DC}^{Ar}	~10^9
Q_{DX}^{NO}	~10^8
Q_{CX}^{NO}	~10^8
Q_P (v' = 0)	1.7 × 10^9
Q_{AX}^{Ar}	10^5–10^6
Q_{AX}^{NO}	10^6–10^7

NO is assumed to self-quench from the D and C states to the X state exclusively.

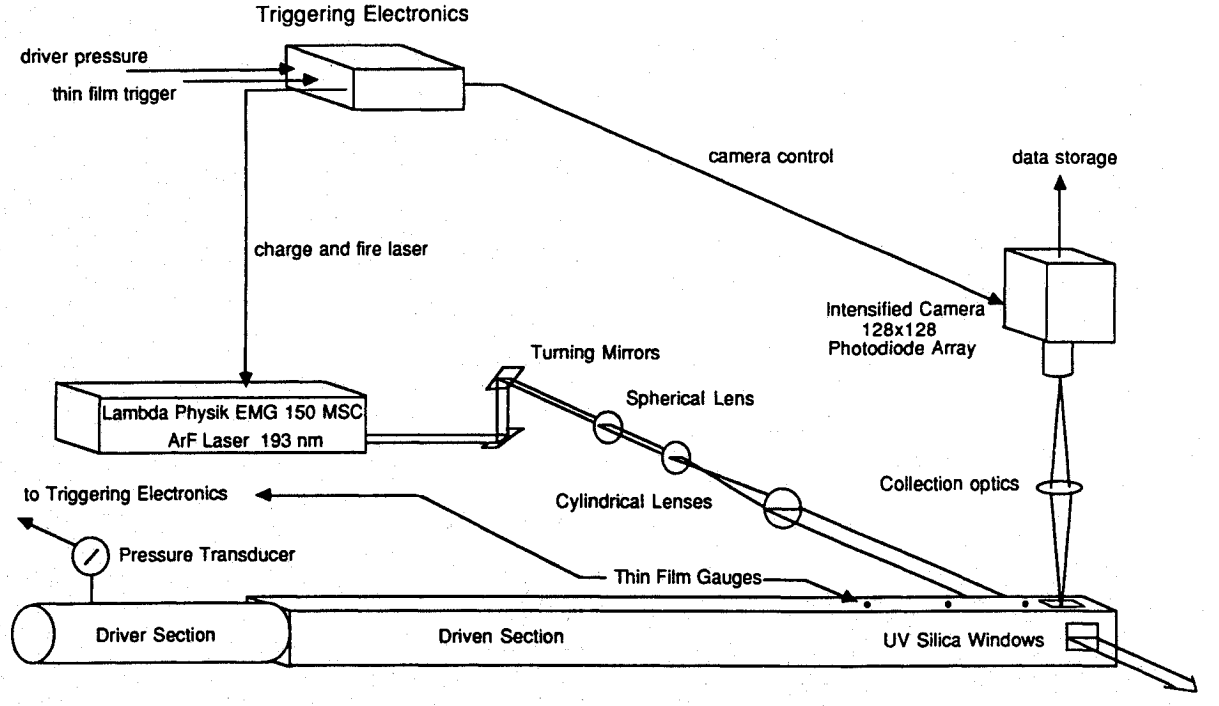

Fig. 3 Schematic of the experimental facility.

Experimental Procedure

Shock Tube

A schematic of the experimental facility is shown in Fig. 3. The flows studied were generated in a 6-m-long shock tube in which the 4.5-m-long driven section had a 3- × 3-in. square cross section. Ultraviolet-grade fused silica windows were mounted flush with the shock-tube walls to provide optical access with minimal flow disturbance. The incident shock-wave velocity was measured across two intervals using standard thin-film gauges located just upstream of the test section. The measured shock velocity was used to calculate the temperature and pressure of the shock-heated gas. The shock tube was evacuated to 5×10^{-5} Torr or lower before each run and the leak rate was 8×10^{-5} Torr/min. Test gas mixtures were obtained by diluting a commercial mixture of 5% NO in argon and were mixed in a cylinder equipped with a magnetic stirrer.

A series of electronic delays was used to sequence the laser firing, intensifier gating, and camera readout. The shock-tube driver pressure was monitored with a transducer that triggered the laser power supply to charge just prior to diaphragm rupture. A thin-film gauge upstream of the test section was used to detect the arrival of the shock wave and to initiate the delay sequence used to trigger the laser/intensifier/camera system.

Laser

A tunable ArF injection-seeded excimer laser (~100 mJ/pulse with ~15 ns pulsewidth) was used as the excitation source. The laser was operated in a narrowband mode (~1 cm^{-1} linewidth) and tuned to excite the $D^2\Sigma^+ \leftarrow X^2\Pi$ (0,1) R_2 (28.5) transition of NO at 193.346 nm. The 6- × 22-mm beam was rotated to a horizontal orientation using two uv turning mirrors and then directed through a spherical lens (f = 2 m) and a pair of cylindrical lenses (f = 150 and 500 mm) to form a sheet approximately 500 μm thick.

Including losses due to room air absorption of the beam and imperfect transmission through the optical elements, the resulting spectral laser intensity in the test section was approximately 10^7 W/cm^2-cm^{-1}. This laser intensity is about five times higher than the saturation intensity measured by Wodtke et al.[10] For the flows considered here, we indeed found evidence of partial saturation; however, as discussed later, the partial saturation observed has no significant impact on the vibrational relaxation measurements presented here.

Although the laser was operated in a narrowband mode, there is a small broadband component to its spectral output. The locking efficiency of the laser, defined as the ratio of the energy within the tunable narrow linewidth to the total pulse energy, was measured to be 85–90% for this wavelength. The locking efficiency was measured by imaging a 5% reflection of the laser beam onto the entrance of a 3/4-m spectrometer operating in seventh order (~0.01-nm resolution). The spectrum was recorded with a 512-element linear photodiode array mounted at the exit plane of the spectrometer. The locking efficiency was determined by comparing the magnitude of the broadband component of the narrowband laser output to that of the laser running broadband (i.e., with the oscillator blocked). The reduction of the broadband component of the output in narrowband operation is a direct measure of the locking efficiency of the laser.[11]

Imaging System

The broadband fluorescence induced from a single laser shot was collected at 90 deg to the illumination plane with a uv-Nikkor lens (f 4.5, 105-mm focal length). A 2-mm-thick BG-24 Schott glass (200-nm long-pass) filter was used to block elastically scattered laser light while transmitting most of the NO fluorescence. The lens was focused using a commercial resolution target. This lens is corrected for aberrations and has significantly better resolution than the camera system (see the following discussion). As a result, the effective depth of field is >10 mm and exact positioning of the laser sheet at the focal plane of the lens is not critical.

The fluorescence was imaged onto a single microchannel plate intensifier (ITT F4111) that was fiber-optically coupled to a Reticon MC9128 camera. This Reticon camera utilizes an array of 128 × 128 pixels (each pixel 60 × 60 μ) and provides frame reset- and acquire-on-demand, an essential characteristic for the timing requirements of this experiment. Image acquisition was performed with a Data Translation DT-2851 frame grabber in a PC/AT compatible computer.

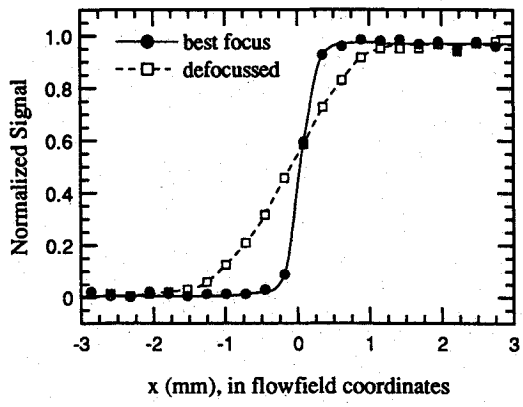

Fig. 4 Knife edge response of the imaging system at best focus and at a severe degree of defocusing: each point represents an individual pixel and corresponds to ~0.27 mm in the object plane.

The intensifier gate width was ~1 μs for these measurements. The imaged region was 39 × 39 mm, but the images were trimmed to 35 × 35 mm for presentation. A background image was subtracted from each of the PLIF images, and a laser sheet correction was applied to account for spatial variations in the input laser intensity profile. The sheet correction was obtained by averaging several images of the equilibrium (and thus uniform) region far downstream of an incident shock. Shot-to-shot variations in the laser intensity profile were found to be generally <10%. Thus, an average sheet correction introduces a slight systematic error; however, this error can be removed if the laser sheet profile is monitored shot by shot with, for example, a linear photodiode array.

Spatial Resolution

Background

The overall spatial resolution of the imaging system is determined by the combination of its three major components: the imaging lens, image intensifier, and two-dimensional photodiode array. The spatial resolution of an imaging system is conventionally described in terms of spatial frequencies, which can be interpreted here as the rate at which the fluorescence signal varies spatially. Large spatial gadients in the fluorescence signal correspond to high spatial frequencies, whereas small gradients correspond to low spatial frequencies. To evaluate the maximum spatial resolution of the imaging system, we must consider both the Nyquist frequency of the array and the cutoff frequency of the system modulation transfer function (MTF).[14] The minimum of these two criteria sets the maximum spatial resolution of the imaging system.

The Nyquist frequency of the array [8.33 line pairs (lp)/mm in the image plane for our camera] is the maximum spatial frequency that can be faithfully reconstructed in an image. Spatial frequencies greater than Nyquist cannot be accurately reconstructed in the image and will be aliased, i.e., recorded (erroneously) as frequencies lower than Nyquist.

By definition, the system MTF is a function of spatial frequency and indicates the ability of an imaging system to reproduce the contrast of an object. Each component in an optical system has a characteristic MTF, and the response of the entire (linear) system is given by the product of the component MTFs. The overall cutoff frequency is typically defined as the spatial frequency at which the system MTF falls to 4%.

For the system used here, the cutoff frequency of the lens is ~150 lp/mm, whereas the cutoff frequencies of the image intensifier and the camera are ~22 and ~17 lp/mm in the image plane, respectively. Thus, it is clear that the image intensifier and the array limit the spatial resolution of this system. If we model the MTF of the intensifier as a Gaussian and that of the array as a sinc function,[14] the overall cutoff frequency of the system is ~15 lp/mm. As a result, at best focus, this optical system will transmit spatial frequencies greater than the array Nyquist frequency and the potential for aliasing exists.

It has been suggested that, when the potential for aliasing exists, the lens should be defocused to reduce the system cutoff frequency to prevent aliasing by the array[15]; however, defocusing the lens will result in a blurring of sharp edges as well as an overall loss in contrast within the image and is generally undesirable. Indeed, if the aliasing does not introduce any significant degradations to the image, a cutoff frequency greater than Nyquist is advantageous because the imaging system will generally have a better overall frequency response and produce a sharper image.

For digital imaging of structures containing sharp edges (e.g., a shock front), the image degradation introduced by aliasing is usually limited to those pixels adjacent to the sharp edge.[15] Therefore, aliasing is a localized effect and pixels elsewhere within the image are not affected. For our imaging system, at best focus, we expect a minimal amount of distortion in the fluorescence profile near the shock front due to aliasing.

Knife Edge Response

We can examine the system spatial resolution and simulate the aliasing introduced into the fluorescence signal near a shock wave by measuring the knife edge response of the system. A knife edge input is a severe test of the system response because the input spectrum of the edge is composed of frequency components far in excess of the Nyquist limit of the array. Thus, it provides a means of simulating the worst case for this study, i.e., the nearly instantaneous jump in fluorescence signal that occurs across a very strong shock wave.

In a knife edge image, pixels on one side of the image will show zero signal and on the other side will show full signal. However, the transition between these regions, i.e., the edge response, will not be perfectly sharp due to imperfections in the collection optics and aliasing introduced by array.[16] For a perfect system with no aliasing, we would expect at least one pixel in the edge response to have an intermediate signal because, for our array, the exact image of the knife edge is more likely to be located within a given pixel, rather than between pixels.

To measure the edge response, we imaged a knife edge positioned at the center of the object plane and back illuminated with a uniform near-white light source. Figure 4 shows the knife edge response for best focus and for a severely degraded focus. At best focus, the resolution is excellent, with the edge response blurred over about three pixels. Preliminary edge response calculations (which do not account for aliasing) indicate that most of the blurring in this case is due to the finite system cutoff frequency. Thus, aliasing appears to be a minor effect here.

The edge response for this system with a large degree of defocusing is also shown in Fig. 4. In this case the lens has been defocused to reduce the system cutoff frequency to <8 lp/mm, thereby ensuring that no aliasing is introduced by the array. Note that the resolution here is degraded considerably, with the edge response extending over about 10 pixels. Hence, we see that defocusing the lens distorts the measured edge response more than the combined effects of aliasing and a finite system response in the best focus case. Therefore, even with the aliasing introduced by the array, adjusting the lens to the best focus provides the optimum spatial resolution for this application.

We can expect similar if not better resolution in the measured fluorescence profile near the shock fronts in the flows examined here. In this study, the $v'' = 1$ level is excited and the resulting fluorescence profile is exponential in nature. As a result, the spatial frequency content of the fluorescence signal is lower than that of a step input; thus, even for very

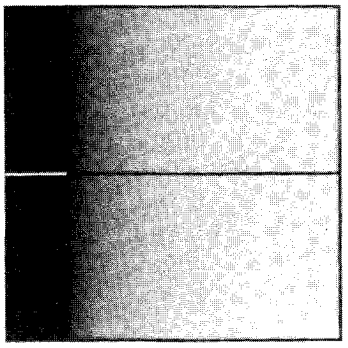

Fig. 5 PLIF image of an incident shock moving from right to left at ~1.24 mm/μs in a 1% NO/argon mixture.

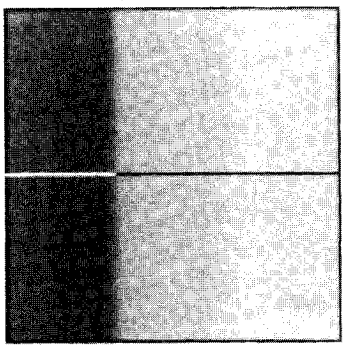

Fig. 7 PLIF image of a reflected shock moving right to left at ~0.66 mm/μs in a 0.5% NO/argon mixture.

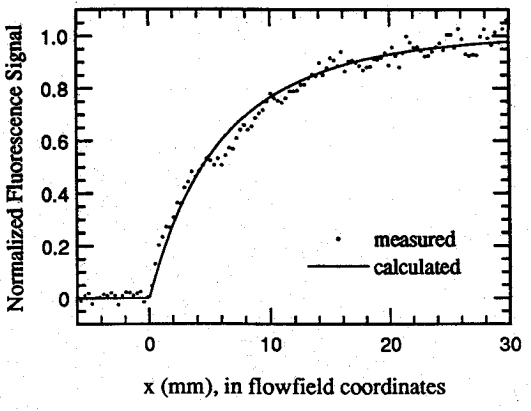

Fig. 6 Comparison of measured and calculated axial fluorescence profiles for the incident shock shown in Fig. 5: each point represents the local average pixel value and corresponds to ~0.31-mm (axial) resolution in the flowfield.

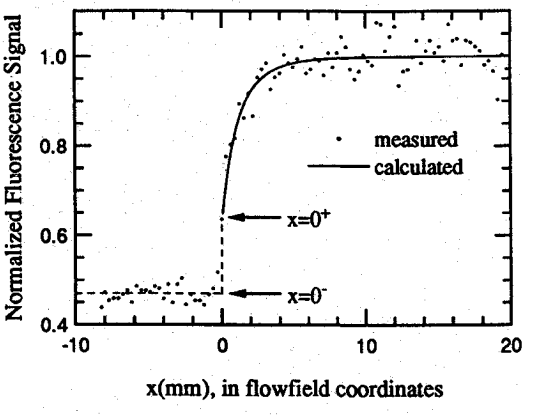

Fig. 8 Comparison of the measured and calculated fluorescence profiles for the reflected shock wave shown in Fig. 7: each point represents an individual pixel and corresponds to ~0.31-mm resolution in the flow coordinates.

strong shocks, the blurring of the shock front should be less severe than that for the knife edge. Further, if any aliasing occurs, it will only affect those pixels adjacent to the shock front and, thus, will not, in general, distort the measured fluorescence profile.

Results and Discussion

Incident Shock

Figure 5 shows a single-shot image of an incident shock moving from right to left at ~1.24 mm/μs in a 1% NO/argon mixture. The image is displayed in a continuous gray scale in which white indicates the highest fluorescence signal and, thus, a larger $v'' = 1$ population. The conditions upstream (left) of the shock are 295 K and 25 Torr, and the equilibrium conditions downstream of the shock are 1640 K and 0.62 atm. For these conditions, no dissociation of NO occurs within the imaged region.

We can examine the vibrational relaxation downstream of the shock by plotting the axial fluorescence distribution. Figure 6 is a plot of the measured axial fluorescence profile obtained by averaging across five pixel rows oriented parallel to the line indicated in Fig. 5. The shock front is located at $x = 0$ in the plot. The fluorescence signal upstream of the shock ($x < 0$) is effectively zero because the absorbing state population there is very low. Downstream of the shock ($x > 0$), the fluorescence signal increases exponentially due to vibrational relaxation, i.e., due to the increasing $v'' = 1$ population. Note that no immediate increase in the fluorescence signal downstream of the shock front results from the rotational relaxation because the initial vibrational population is so low.

Figure 6 also shows the normalized calculated fluorescence profile given by

$$\frac{S_f(x)}{S_f^*} = \frac{F[T_v(x)]}{F[T_v^*]} \tag{2}$$

where x is the axial coordinate, S_f the (temporally integrated) fluorescence signal, and the superscript (*) indicates the equilibrium value behind the shock front. To model the fluorescence, the absorbing state population was calculated assuming an (essentially) instantaneous rotational relaxation at the shock front and an exponential vibrational relaxation downstream of the shock. The normalized axial fluorescence profile for $x > 0$ can be modeled using Eq. (2) because the signal variation downstream of the shock is primarily determined by the variation in the absorbing state vibrational population. Note that here we are neglecting the very slight variation in both the translational/rotational temperature and the number density downstream of the shock, which results from the vibrational relaxation. Also note that the quenching and any optical saturation effects are uniform throughout the region downstream of the shock and need not be considered in this analysis.

For the conditions of the incident shock shown in Fig. 5, laser absorption was <5% across the image and introduced no significant distortion into the measured fluorescence profile. The best fit between the calculated and the measured fluorescence profile for this case was obtained for an overall (i.e., for a vibrational energy) relaxation rate coefficient of 8.9×10^9 cm^3/mol-s, or equivalently, a relaxation time of 24 μs (particle time). This rate is in good agreement with that

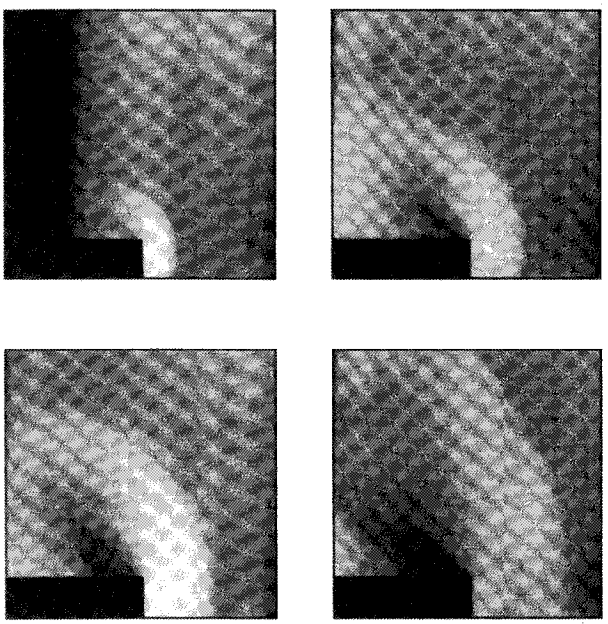

Fig. 9 PLIF images of the development of high-temperature supersonic flow over a two-dimensional plate with a flat nose: a) acquired a few microseconds after the incident shock impinged on the plate and the incident shock is still within the image; b) time delay of 12.5 μs; c) time delay of 25 μs; d) time delay of 62.5 μs.

of Kamimoto and Matsui,[7] who reported a rate that was ~20% faster for these conditions.

Reflected Shock

Figure 7 shows a single-shot image of a reflected shock moving from right to left at ~0.66 mm/μs in a 0.5% NO/argon mixture. The equilibrium conditions upstream (left) of the shock are 1640 K and 0.62 atm, whereas the equilibrium conditions downstream of the shock are 3450 K and 3 atm. As in the incident shock case, no significant dissociation of NO is expected within the imaged region.

Figure 8 shows the measured axial fluorescence profile obtained from the reflected shock image. The data shown were obtained from the single pixel row highlighted in Fig. 7. The scatter results primarily from shot noise and indicates that the signal-to-noise ratio in the image is ~10. The shock front is located at $x = 0$. Fluorescence signal is observed both upstream and downstream of the reflected shock because both regions have significant $v'' = 1$ populations. The higher fluorescence signal downstream of the shock ($x > 0$) results both from a higher number density and from a higher vibrational temperature in that region. The uniform signal upstream of the shock ($x < 0$) indicates that the gas in that region has fully equilibrated, as expected. In contrast, vibrational relaxation is observed downstream of the shock, although equilibrium is reached in <10 mm. For the conditions of this reflected shock, laser attenuation was <10% across the image and introduced no significant distortion into the measured fluorescence profile.

Figure 8 also shows the calculated downstream fluorescence profile for these conditions, assuming an overall relaxation rate of ~2.24×10^{10} cm^3/mol-s (i.e., a relaxation time of ~4 μs). This rate is also in good agreement with that of Kamimoto and Matsui,[7] who reported a rate that was ~20% faster for these conditions.

The fluorescence profile in Fig. 8 was calculated using Eq. (2), which only (strictly) applies for $x > 0$, as discussed earlier. Note that just downstream of the shock (at $x = 0^+$), prior to any rotational or vibrational relaxation, the translational temperature, number density, collisional quenching rates, and effective saturation intensity increase due to the shock compression. Consequently, the fluorescence signal measured at $x = 0^+$ will not, in general, equal the fluorescence signal prior to the shock compression at $x = 0^-$. Similarly, the normalized fluorescence signal calculated at $x = 0^+$ using Eq. (2) will not, in general, equal the normalized fluorescence signal measured at $x = 0^-$. Because the fluorescence signal calculated at $x = 0^+$ is greater than the fluorescence signal measured at $x = 0^-$, we can conclude that, for this case, the shock compression acts to increase the baseline fluorescence signal for $x > 0$.

The agreement among all of our measured relaxation rates and those previously reported is excellent, even though we made no attempt to remove the trace impurities (e.g., water vapor, NO_2, and N_2O) expected in our test gas. Although it is well known that triatomic impurities can significantly increase the relaxation rate for diatomic molecules, the apparent insensitivity of NO to impurities in our test gas may be due to the fact that NO relaxes anomolously fast compared to other diatomic gases.

Supersonic Flow over a Blunt Body

Figures 9 show a four-image sequence of the development of high-temperature supersonic flow over a two-dimensional plate with a flat nose. The flow in these images is moving from right to left. The images shown were obtained in four separate experiments in which the time delay prior to triggering the imaging system was increased in each run, to simulate the temporal evolution of this flow. The shot-to-shot variations in the flow conditions were <2%. The geometry as well as the characteristic features[17] of this flow in the fully developed stage are shown schematically in Fig. 10. The test gas in these images was 5% NO in argon and the incident shock velocity was 1.04 mm/μs. The freestream Mach number was 1.11 and the equilibrium freestream temperature and pressure were 1200 K and 0.85 atm, respectively. The images are shown in a continuous gray scale, with white indicating the highest signal.

The image in Fig. 9a was acquired only a few microseconds after the shock impinged on the plate. As a result, the incident shock is still within the imaged region. A detached bow shock has already formed and is clearly visible in the image. The gas downstream of the bow shock shows a higher fluorescence signal due to its higher number density and vibrational temperature.

In the subsequent images, the incident shock has propagated out of the field of view. As the time sequence progresses, the bow shock gradually moves farther upstream (i.e., away) from the stagnation point of the plate. In addition, the downstream portion of the bow shock propagates laterally away from the plate. In Fig. 9d, the bow shock has nearly reached its equilibrium position.

As the gas downstream of the shock flows around the nose of the plate, the boundary layer separates. A short distance downstream of the nose, the boundary layer reattaches and a shock is generated to turn the flow parallel to the plate. The shock generated at the reattachment point is clearly visible in Figs. 9b–9d, and the sequence shows that the reattachment point moves downstream as the flow develops. As before, the signal increases downstream of this shock wave due to an increase in the vibrational temperature of the gas. Also, we note that the lower signal in the region surrounding the recirculation zone (where the boundary layer has separated) is most likely due to the expansion of the flow as it curves around the recirculation zone.

The images presented in Figs. 9 clearly demonstrate the potential of PLIF imaging as a diagnostic technique for investigating complex, high-temperature supersonic flows. In the flows examined here, the interpretation of the fluorescence signal was relatively straightforward because these flows are well understood. In general, however, the interpretation of individual images may not be as straightforward because

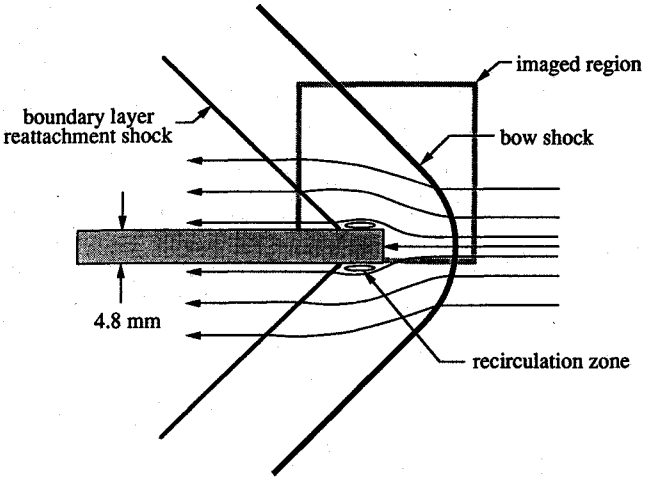

Fig. 10 Schematic illustrating the imaging geometry and the characteristic features of supersonic flow over a two-dimensional plate with a flat nose.

the fluorescence signal changes with variations in number density, rotational and vibrational temperatures, species concentration, laser intensity, and various collisional quenching rates.

In more complex flows, multiple-wavelength excitation/detection techniques can be employed to isolate the particular flowfield property of interest.[1,2] For example, the vibrational temperature can be obtained by exciting transitions from two different ground state vibrational levels to the same upper electronic state vibrational level. By dividing the resultant fluorescence images, the dependence on all parameters other than the vibrational temperature is removed in the processed image. Similar schemes can be devised to isolate other flowfield properties of interest.

Conclusions

Single-laser-shot PLIF images of NO in shock-heated flows with vibrational nonequilibrium have been presented, and the importance of spatial resolution for properly imaging the fluorescence signal near shock waves has been discussed in detail. The variation in fluorescence signal in the images presented reflects the evolving population of the $v'' = 1$ vibrational level in the ground electronic state; as a result, the signal can be readily used to investigate vibrational nonequilibrium in the ground electronic state. The vibrational relaxation of NO diluted in argon was examined in images of both planar incident and reflected shocks, and the agreement with previously reported relaxation rates was excellent.

A four-image sequence illustrating the temporal evolution of high-temperature supersonic flow over a two-dimensional blunt body was also presented. The images clearly reveal the shock-wave structure through the combined variation of number density and vibrational temperature in the flowfield. The demonstration of single-shot PLIF imaging of NO in transient supersonic flows with vibrational nonequilibrium is of considerable importance because NO is a species present in many important aerodynamic applications. These results confirm that single-shot PLIF imaging is a promising diagnostic technique for transient flow facilities because it provides species-specific and quantum-state-specific measurements throughout the flowfield with excellent spatial and temporal resolution.

Acknowledgments

This research was supported by the U.S. Air Force Office of Scientific Research, Aerospace Sciences Directorate, with Julian Tishkoff as Technical Monitor. The authors would like to acknowledge P. H. Paul and J. M. Seitzman for their important contributions to this work.

References

[1]Hanson, R. K., "Combustion Diagnostics: Planar Imaging Techniques," *Twenty-First Symposium (International) on Combustion*, Combustion Inst., Pittsburgh, PA, 1986, pp. 1677–1691.

[2]Hanson, R. K., Seitzman, J. M., and Paul, P. H., "Planar Laser-Fluorescence Imaging of Combustion Gases," *Applied Physics B*, Vol. 50, No. 6, 1990, pp. 441–454.

[3]Paul, P. H., Seitzman, J. M., Lee, M. P., McMillin, B. K., and Hanson, R. K., "Planar Laser-Induced Fluorescence Imaging of Supersonic Flows," AIAA Paper 89-0059, Jan. 1989.

[4]McMillin, B. K., Lee, M. P., Paul, P. H., and Hanson, R. K., "Planar Laser-Induced Fluorescence Imaging of Nitric Oxide in a Shock Tube," AIAA Paper 89-2566, July 1989.

[5]McMillin, B. K., Lee, M. P., Palmer, J. L., Paul, P. H., and Hanson, R. K., "Planar Laser-Induced Fluorescence Imaging of Shock-Heated Flows in Vibrational Nonequilibrium," *Flow Visualization—1989*, edited by B. Khalighi, M. J. Brown, and C. J. Freitas, FED Vol. 85, American Society of Mechanical Engineers, New York, 1989, pp. 55–62.

[6]Moser, L. K., and Hindelang, F. J., "Vibrational Relaxation of NO Behind Shock Waves," *Experiments in Fluids*, Vol. 7, No. 1, 1989, pp. 67–69.

[7]Kamimoto, G., and Matsui, H., "Vibrational Relaxation of Nitric Oxide in Argon," *Journal of Chemical Physics*, Vol. 53, No. 10, 1970, pp. 3987–3989.

[8]Eckbreth, A. C., "Laser Diagnostics for Combustion Temperature and Species," *Energy and Engineering Science Series*, edited by A. K. Gupta and D. G. Lilley, Vol. 7, Abacus, Cambridge, MA, 1988, pp. 301–361.

[9]Shibuya, K., and Stuhl, F., "Single Vibronic Emissions from NO $B^2\Pi(v' = 7)$ and O_2 $B^3\Sigma_u$ $(v' = 4)$ Excited by 193 nm ArF Laser," *Journal of Chemical Physics*, Vol. 76, No. 2, 1982, pp. 1184–1186.

[10]Wodtke, A. M., Huwel, L., Schluter, H., Meijer, G., Andresen, P., and Voges, H., "High-Sensitivity Detection of NO in a Flame Using a Tunable ArF Laser," *Optics Letters*, Vol. 13, No. 10, 1988, pp. 910–912.

[11]Wodtke, A. M., Huwel, L., Schluter, H., and Andresen, P., "Simple Way to Improve a Tunable Argon Fluoride Laser," *Review of Scientific Instruments*, Vol. 60, No. 4, 1989, pp. 801–802.

[12]Callear, A. B., and Pilling, M. J., "Fluorescence of Nitric Oxide: Part 7," *Transactions of the Faraday Society*, Vol. 66, No. 571, 1970, pp. 1618–1634.

[13]Callear, A. B., and Pilling, M. J., "Fluorescence of Nitric Oxide: Part 6," *Transactions of the Faraday Society*, Vol. 66, No. 571, 1970, pp. 1886–1906.

[14]Kychakoff, G., Howe, R. D., and Hanson, R. K., "Quantitative Flow Visualization Technique for Measurements in Combustion Gases," *Applied Optics*, Vol. 23, No. 5, 1984, pp. 704–712.

[15]Barbe, D. F., and Campana, S. B., "Aliasing and MTF Effects in Photosensor Arrays," *Solid State Imaging*, edited by O. P. G. Jespers, F. van de Wille, and M. H. White, Noordhoof, Leiden, The Netherlands, 1976, pp. 623–636.

[16]Williams, C. S., and Becklund, O. A., *Introduction to the Optical Transfer Function*, Wiley, New York, 1989.

[17]Mair, W. A., "Experiments on Separation of Boundary Layers on Probes in Front of Blunt-Nose Bodies in a Supersonic Air Stream," *Philosophical Magazine*, Vol. 43, Ser. 7, No. 342, 1952, pp. 695–716.